

ORIGINAL ARTICLE

# Postmortem Magnetic Resonance Imaging to Guide the Pathologic Cut: Individualized, 3-Dimensionally Printed Cutting Boxes for Fixed Brains

Martina Absinta, MD, Govind Nair, PhD, Massimo Filippi, MD, Abhik Ray-Chaudhury, MD, Maria I. Reyes-Mantilla, MD, Carlos A. Pardo, MD, and Daniel S. Reich, MD, PhD

## Abstract

Interfacing magnetic resonance imaging (MRI) with pathology is critically important for understanding the pathologic basis of MRI signal changes in vivo and for clinicopathologic correlations. Postmortem MRI is an intermediate step in this process; unfortunately, however, relating the data to standard pathologic sections, which are relatively thick and often nonparallel, is both time-consuming and insufficiently accurate. The aim of this project was to develop technology to integrate postmortem, high-resolution, whole-brain MRI into the planning and execution of pathologic analysis through precise localization of the target and coordinates of cut. Compared with standard pathologic sectioning, the use of an individualized, 3-dimensionally printed cutting box—designed based on postmortem MRI of formalin-fixed whole brains—improved the speed, quality, and accuracy of radiologic-pathologic correlations and, specifically, the histopathologic localization of imaging findings. The technology described herein is easily implemented, applicable to any brain disorder, and potentially extendable to other organs. From the point of view of the pathologist, this technique can improve localization of small or subtle abnormalities, whereas from the point of view of the radiologist, it has the potential to improve understanding of MRI signal changes observed in diseases.

**Key Words:** Cutting box, High resolution, MRI-Pathology correlations, Postmortem MRI.

From the Translational Neuroradiology Unit (MA, GN, DSR) and Surgical Neurology Branch (AR-C), National Institute of Neurological Disorders and Stroke, National Institutes of Health; and Department of Neurology, Johns Hopkins School of Medicine (MIR-M, CAP, DSR), Baltimore, Maryland; and Neuroimaging Research Unit, Institute of Experimental Neurology, Division of Neuroscience, San Raffaele Scientific Institute, Vita-Salute San Raffaele University, Milan, Italy (MA, MF).

Send correspondence and reprint requests to: Daniel S. Reich, MD, PhD, Translational Neuroradiology Unit, National Institute of Neurological Disorders and Stroke, National Institutes of Health, 10 Center Drive MSC 1400, Building 10 Room 5C103, Bethesda, MD 20892; E-mail: daniel.reich@nih.gov

Martina Absinta and Govind Nair contributed equally to this work.

The Intramural Research Program of the National Institute of Neurological Disorders and Stroke supported this study. Carlos A. Pardo and Maria I. Reyes-Mantilla were supported by the Bart McLean Fund for Neuroimmunology Research—Project Restore at Johns Hopkins University School of Medicine.

Supplemental digital content is available for this article. Direct URL citations appear in the printed text and are provided in the HTML and PDF versions of this article on the journal's Web site ([www.jneurol.com](http://www.jneurol.com)).

## INTRODUCTION

There is a growing need for interfacing brain morphology with magnetic resonance imaging (MRI) to improve understanding of the pathologic basis of MRI signal changes and thereby validate in vivo surrogates of physiologic and pathologic processes (1–5). Postmortem MRI is a valuable intermediate step toward this end. In particular, it acts as a bridge from in vivo images to pathologic examination. In this multimodal context, pioneering experience in combining digitalized whole-mount histology and MRI has been recently realized for the whole brain of H.M., a famous patient with epilepsy (6), suggesting that MRI might constitute the topographic baseline reference for the 3-dimensional (3D) histopathology of the future (7). In cases where whole-brain histopathology is not required or feasible, in vivo and postmortem MRI can be used as a guide for limited pathologic sampling, thereby saving valuable resources (8–10). Similarly, in forensic radiology, postmortem MRI has been recognized as a supplementary diagnostic tool that is able not only to provide a general overview of the corpse but also to uncover small findings and to address specific forensic questions (11, 12). In this setting, the term “virtual autopsy” has been recently proposed as a topic for future research (13).

At this time, however, the tools that are required for precise colocalization are not routinely used in pathologic examinations (14). In general, sectioning of the brain, either coronally, sagittally, or horizontally, leads to large variations in slab thickness and in the degree to which slab faces remain parallel. In addition, subsequent sampling of small tissue blocks for in-depth histological analysis is frequently blind to findings, particularly small findings that are not visible on the slab surface after the initial cut. Integrating and comparing data derived from the standard procedure with in vivo and postmortem MRI are time-consuming and often not sufficiently accurate.

The aim of this project was to develop a technology to integrate postmortem, high-resolution, whole-brain MRI into the planning and execution of pathologic analysis through precise localization of the target structure and cutting coordinates. There are several reasons why postmortem MRI acquisition is preferentially performed on the whole fixed brain rather than on tissue slabs. These include fewer artifacts (air bubbles and distortion at slab edges), preserved landmarks for radiologic interpretation, and reduced total scan

time to cover the whole brain. In addition, whole-brain acquisition allows construction of a customized, 3-dimensionally printed, brain-slicing box—the main innovation proposed herein. Based on our results, we propose that in vivo and post-mortem high-resolution MRI can help to guide pathology studies, particularly in the research setting.

## MATERIALS AND METHODS

### Tissue Samples

Three autopsy brains were obtained with consent from the next of kin. Clinical information and in vivo MRI scans were obtained under an Institutional Review Board–approved clinical research protocol and compared with postmortem data for Patient 1. Similarly, clinical information and in vivo MRI scans were obtained from Patients 2 and 3 as part of clinical-pathologic studies under an autopsy protocol at Johns Hopkins Hospital (Baltimore, MD).

Patient 1 was a 59-year-old man with primary progressive multiple sclerosis (MS) with disease duration (i.e. time from symptom onset to death) of 21 years. The cause of death was respiratory distress and sepsis following multiple embolic strokes. Patient 2 was a 55-year-old woman with secondary progressive MS with disease duration of more than 20 years; the cause of death was pneumonia. Patient 3 was a 22-year-old woman with anti-*N*-methyl-D-aspartate receptor encephalitis that was not responsive to intravenous steroids, plasma exchange, intravenous immunoglobulin, or rituximab. The disease duration was approximately 6 months, and the cause of death was sudden cardiac arrest likely secondary to dysautonomia.

Postmortem-autopsy intervals were 5 hours (Department of Pathology, UPMC Presbyterian, Pittsburgh, PA), 28 hours (Johns Hopkins Hospital), and 7 hours (Johns Hopkins Hospital), respectively. The brains were extracted en bloc and subsequently fixed by immersion in 10% formalin for 2 weeks. After MRI at the National Institutes of Health (Bethesda, MD), sectioning was performed using a customized cutting box (described later) for Patients 1 and 3 and using standard procedures for Patient 2 (Table).

### Postmortem 7-T MRI

The formalin-fixed forebrain was first separated from the brainstem and cerebellum by cutting along a transversal plane passing through the midbrain at the level of the substantia nigra.

The forebrain was then positioned within an imaging container consisting of a cylindrical tube with 25 cm inner diameter, 30 cm length, and 0.5 cm wall thickness (Fig. 1A). The container was fitted with a hemispheric dome at one end for optimal magnetic susceptibility characteristics and a sealable spout at the other end for filling and applying suction. The shape of the container was such that it optimally fit the volumetric receive coil used on the 7-T MRI scanner; the brain was positioned approximately at the center of the transmit coil. The container was filled with Fomblin (Solvay Solexis, West Deptford, NJ), a perfluoropolyether that is susceptibility-matched to tissue, thereby reducing artifacts in images. Air bubbles were removed through the spout by gentle suctioning for approximately 30 minutes.

Postmortem MRI was performed on a 7-T actively shielded scanner (Siemens, Erlangen, Germany) equipped with a birdcage-type transmit coil and a 32-channel receive coil. The following pulse sequences were executed:

1. Three-dimensional T1-weighted magnetization-prepared rapid gradient echo (T1-MPRAGE) with repetition time of 2,200 milliseconds, echo time of 3.04 milliseconds, inversion time of 1,050 milliseconds, flip angle of 7°, nominal resolution of  $0.6 \times 0.6 \times 0.6$  mm, and 176 coronal slices. The acquisition time for the sequence was 6 minutes 35 seconds.
2. Three-dimensional high-resolution multigradient echo (GRE) T2\* sequence with repetition time of 60 milliseconds; echo times of 6.09, 15.99, 25.89, and 35.79 milliseconds; 4 averages; 88 slices; flip angle of 10°; acquisition time of 2 hours 15 minutes per 36-mm slab; and nominal resolution of  $0.42 \times 0.42 \times 0.42$  mm. Four coronal slabs with 20% overlapping slices were acquired to cover the whole brain.
3. Three-dimensional high-resolution fast low-angle shot T1-weighted sequence with repetition time of 1,000 milliseconds, echo time of 2.71 milliseconds, inversion time of 150 milliseconds, 4 averages, 192 slices, flip angle of 10°, acquisition time of 2 hours 45 minutes per 60-mm slice, and nominal resolution of  $0.31 \times 0.31 \times 0.31$  mm. Three coronal slices with 20% overlapping slices were acquired to cover the whole brain.

All imaging slices were aligned parallel to a coronal plane passing through the mammillary bodies. Images acquired in multiple slabs covering the whole brain were stitched together using their DICOM information, and postprocessing algorithms were developed using AFNI. The typical scan time for the entire

**TABLE.** Summary of Sectioning and Histologic Procedures

Patient No.	Diagnosis	Sectioning Procedure	Histology	MRI Comparison
1	MS	Forebrain with cutting box (twenty-three 6-mm-thick coronal slabs)	Block 1 left temporal lobe (1 × 3-in glass slides)	Immediate and accurate (block sectioned according to MRI coordinates)
		Brainstem-cerebellum with cutting box (nine 6-mm-thick transversal slabs)	NA	NA
2	MS	Forebrain without cutting box (fifteen ~1-cm-thick coronal slabs)	Block 2 left frontal lobe (2 × 3-in glass slides)	A posteriori (3D reformatting of the acquired images was necessary)
3	Anti- <i>N</i> -methyl-D-aspartate receptor encephalitis	Forebrain with cutting box (twenty-one 6-mm-thick coronal slabs)	Block 3 left hippocampus (1 × 3-in glass slides)	Immediate and accurate (block sectioned according to MRI coordinates)

NA, not available.

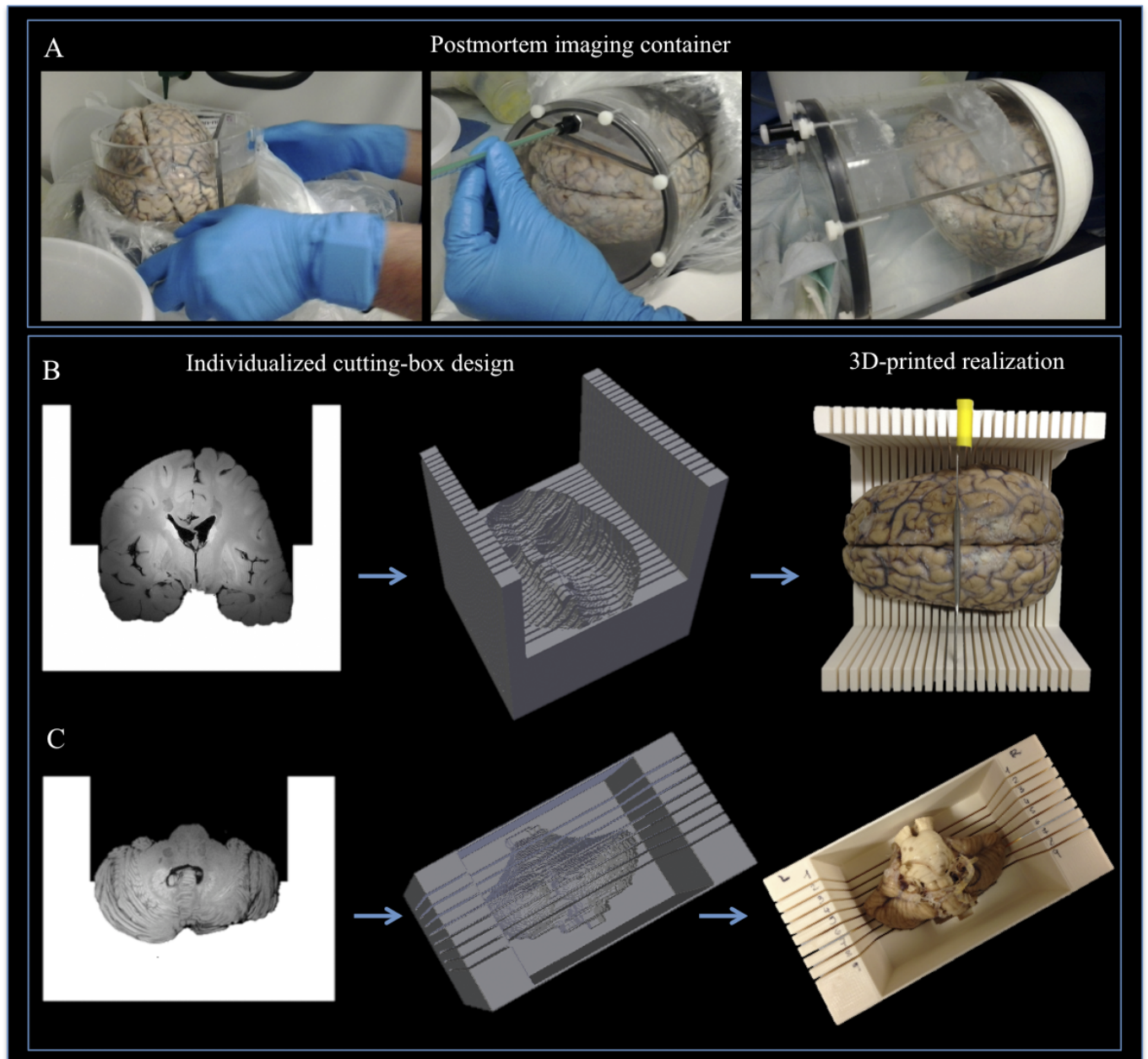


**FIGURE 1.** Illustration of the technique. **(A–C)** A dome-shaped container was fashioned for MRI of the postmortem brain; it was customized to reduce susceptibility artifacts and to fill a 7-T MRI receive coil **(A, left)**. The postmortem brain was immersed in Fomblin and aspirated for air bubbles through the spout by applying suction for approximately 30 minutes before imaging **(A, middle and right)**. For Patient 1, individualized cutting boxes were designed and 3-dimensionally printed for the forebrain **(B)** and brainstem-cerebellum **(C)**. The surface of the fixed brain was rendered from the MRI sequence, and a mold was created to conform to the inferior surface of the brain **(B)** and the posterior surface of the cerebellum **(C)**.

brain was about 17 hours, although only the approximately 6.5-minute T1-MPRAGE scan was used for the preparation of the cutting box.

### Individualized Cutting Box

Three-dimensional T1-MPRAGE images were initially processed using MIPAV (Medical Image Processing, Analysis, and Visualization; National Institutes of Health) to generate the design for the individualized cutting box for each brain.

According to specific findings of interest, the number, position, and thickness of each slab were determined a priori using MRI data. The surface of the forebrain was rendered, and a mold was created to conform to the inferior (skull base) surface (Fig. 1B). To implement this, we thresholded the coronal 3D T1-MPRAGE (Figure, Supplemental Digital Content 1, parts A, B, left column, <http://links.lww.com/NEN/A612>) to obtain the brain mask (Figure, Supplemental Digital Content 1, part A, center, <http://links.lww.com/NEN/A612>). Parallel, coronally



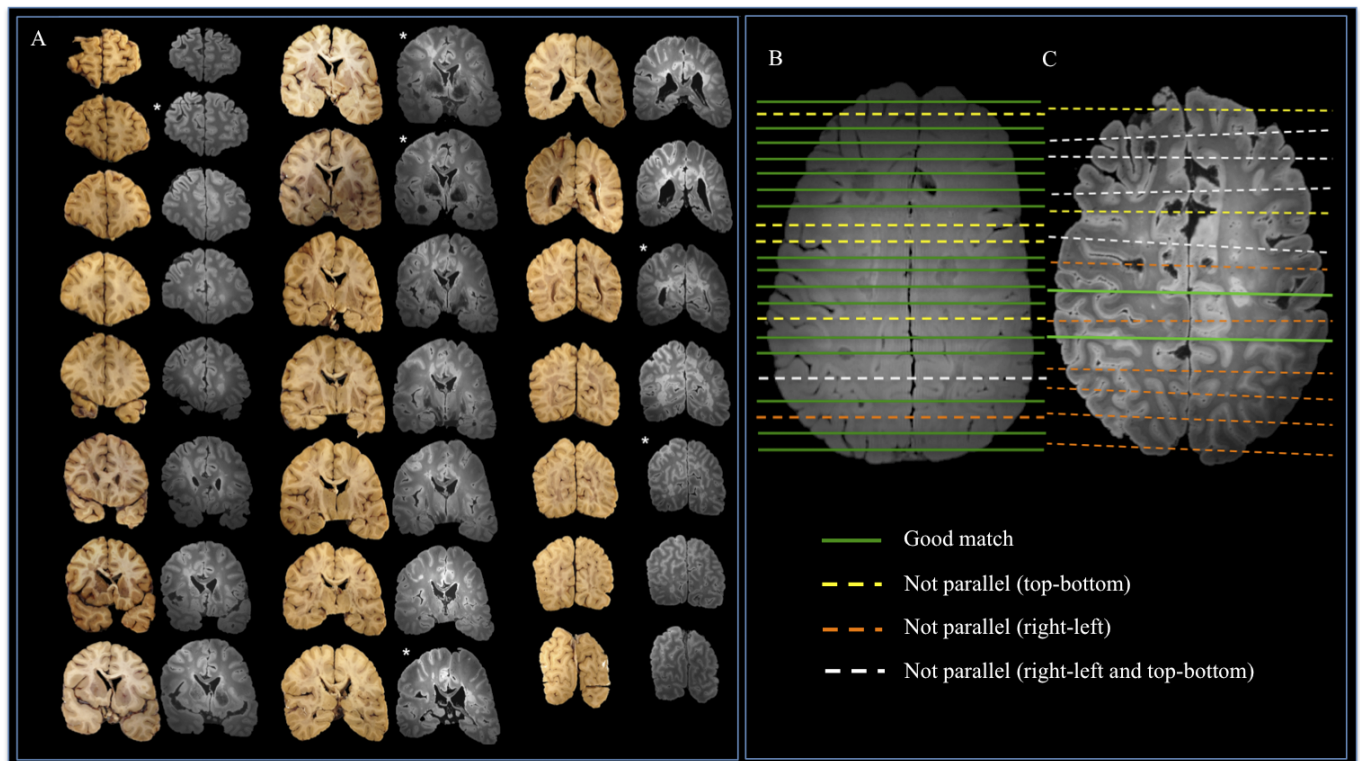


**FIGURE 2.** Comparison of sectioning performance with and without the cutting box. **(A)** Comparison of the gross appearance of brain slabs (anterior surface, starting from Slice 2) and the corresponding coronal GRE (second echo) MRI slices of the brain of Patient 1. \*Areas where the match was judged to be less accurate. **(B, C)** The cutting lines and their accuracy with the cutting box for Patient 1 **(B)** and without the cutting box for Patient 2 **(C)** are superimposed on an axial MRI slice. The sectioning is much less accurate with the traditional cutting method **(C)**.

oriented, 1.2-mm-wide gaps were introduced to accommodate a brain-cutting knife and were placed every 4.8 mm by erasing the corresponding portion of the mask (Figure, Supplemental Digital Content 1, part A, center, B, <http://links.lww.com/NEN/A612>), yielding twenty-four 6-mm-thick slabs from Patient 1 and twenty-two 6-mm-thick slabs from Patient 3. The superior half of the mask was then removed at the level of the maximal right-left span; this left behind a mask of the inferior skull base surface of the brain (Figure, Supplemental Digital Content 1, part A, <http://links.lww.com/NEN/A612>). This partially masked image was then inverted to obtain the shape of the cutting box (Figure, Supplemental Digital Content 1, parts A, B, right column, <http://links.lww.com/NEN/A612>). An accurate cleaning of residual voxels belonging to the parenchyma or ventricles was performed manually. Because this process can be easily copied and repeated for all slices in 3D T1-MPRAGE using image processing algorithms such as MIPAV, the 2-dimensional (2D) design of a brain-cutting box can be generated within 2 hours. Coronal, sagittal, and transversal views of the cutting box design from Patient 1 are shown in Figure, Supplemental Digital Content 1, part C, <http://links.lww.com/NEN/A612>. The surface of the cutting box (2D design) was then 3-dimensionally rendered using OsiriX v5.6 (3D surface rendering tool; <http://www.osirix-viewer.com/>) and saved as .stl (surface tassellation language, a 3D file format compatible with 3D design software and 3D printers).

The cutting box was printed by a 3D printer (Stratasys Dimension Elite, Fortus 360mc; Stratasys, Eden Prairie, MN) in approximately 100 hours. The material used to make the cutting box (cost ~US\$400) included a plastic polymer (acrylonitrile butadiene styrene) and a support material (terpolymer of methacrylic acid, styrene, and butylacrylate) that was dissolved in a hot water solution of NaOH in approximately 24 hours. Using fused deposition modeling technology, the 3D printer extruded and deposited the molten plastic polymer and the support material in layers to build the object from the bottom up. The layer resolution implemented was 0.007 in.

Before accommodating the fixed brain within the cutting box, we smoothed the inner surface of the box using a rotating sandpaper tool (Dremel tools; Robert Bosch Tool Corporation, Mt Prospect, IL) to prevent possible tissue damage.

### Sectioning Procedure

Sectioning was performed by 2 neuropathologists. After the brain had been placed within the cutting box, the slabs were cut consecutively from the center (Fig. 1B) toward the occipital lobe and subsequently toward the frontal lobe. Slabs were removed and labeled immediately after cutting. For comparison, the second brain was cut according to the traditional procedure, without a cutting box (14); this yielded 15 approximately 1-cm-thick slabs.

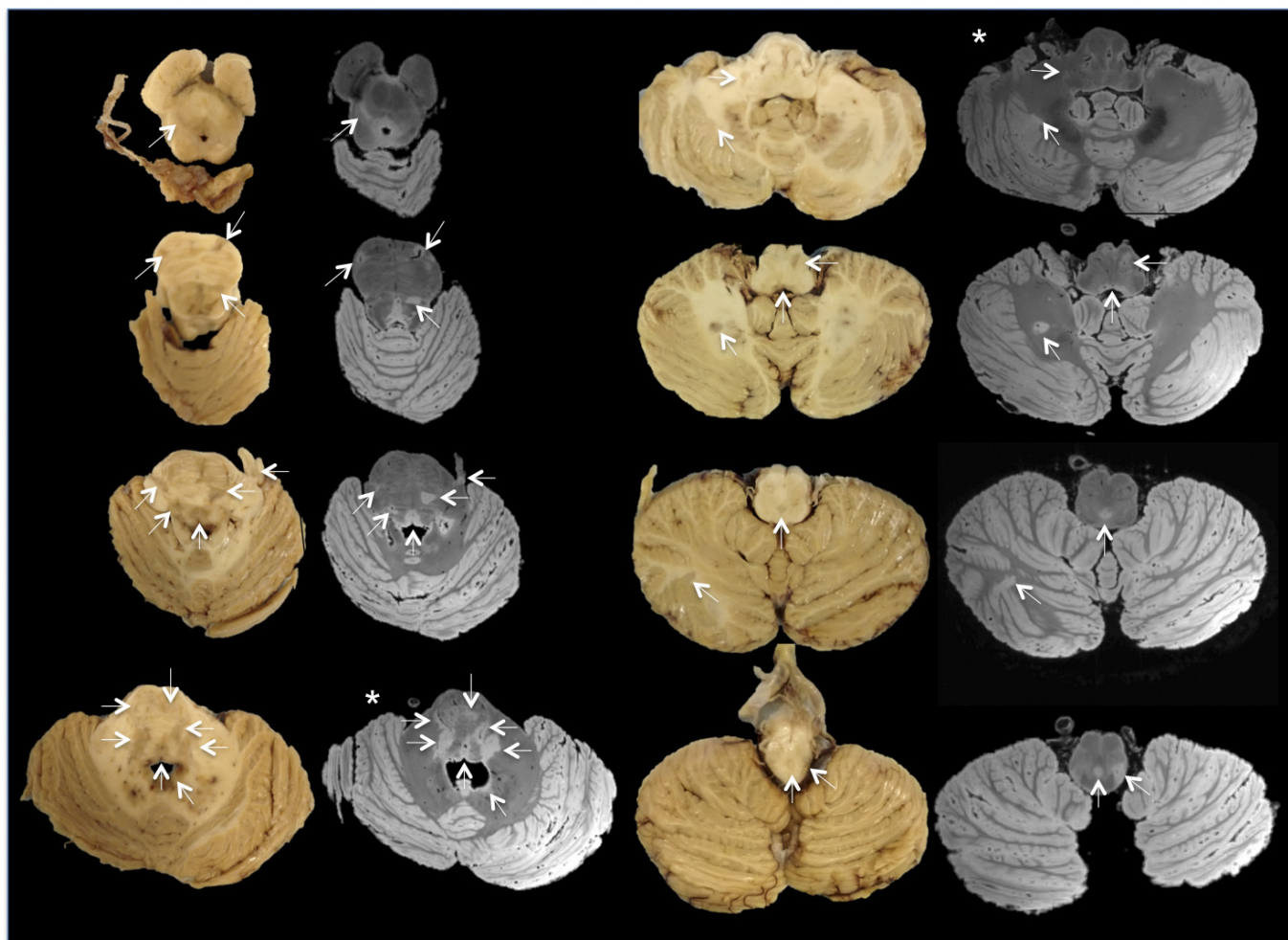


**FIGURE 3.** Brainstem-cerebellum sectioning performance with the cutting box. Matches between the gross appearance of slabs (left) and the corresponding transversal GRE (second echo) MRI slices of the brainstem-cerebellum are shown for Patient 1. White arrows indicate demyelinated lesions; in several of them, the central vein is prominent on the GRE MRI sequence. \*Areas where the match was judged to be less accurate.

### Qualitative MRI-Pathology Matching

The quality of the match between the gross anatomy of the slabs and the coronal T1-MPRAGE data was determined visually according to cortical and ventricular profiles upon the agreement of 2 evaluators (Martina Absinta and Govind Nair). The match was judged to be unsatisfactory when the superior and inferior (and/or right and left) edges spanned several T1-MPRAGE slices, indicating a mismatch of more than 0.5 mm. The 3D high-resolution MRI sequences (GRE and fast low-angle shot) were planned using the same slices as the T1-MPRAGE, so information was naturally linked in the DICOM image files, and as such the correspondence of the high-resolution MRI sequences naturally followed from the correspondence of the T1-MPRAGE to the slab surfaces. To refine the match, we corrected distortions arising from tissue fixation and MRI acquisition using 2D registration between digitized gray scale photos of the brain slab surfaces and corresponding MRI slices. The method of registration was affine (linear, 12 degrees of freedom), followed by a

landmark thin-plate registration in MIPAV (Figure, Supplemental Digital Content 2, <http://links.lww.com/NEN/A613>).

### Brainstem-Cerebellum

To assess the performance of our approach in a more difficult situation, we repeated the same procedure in Patient 1 to make a cutting box for the brainstem-cerebellum (Fig. 1C), yielding nine 6-mm-thick transversal slabs parallel to a plane passing through the middle cerebellar peduncles. After the brainstem-cerebellum had been placed within the cutting box, the slabs were cut consecutively in the craniocaudal direction, and comparison with the postmortem MRI was made according to the cerebellar cortex profile and the surface of the brainstem.

### Histology

Block 1 was obtained from Patient 1. The selected formalin-fixed tissue block from the left temporal lobe was immersed in 30% sucrose at 4°C for approximately 2 days for cryoprotection and then embedded with optimal cutting



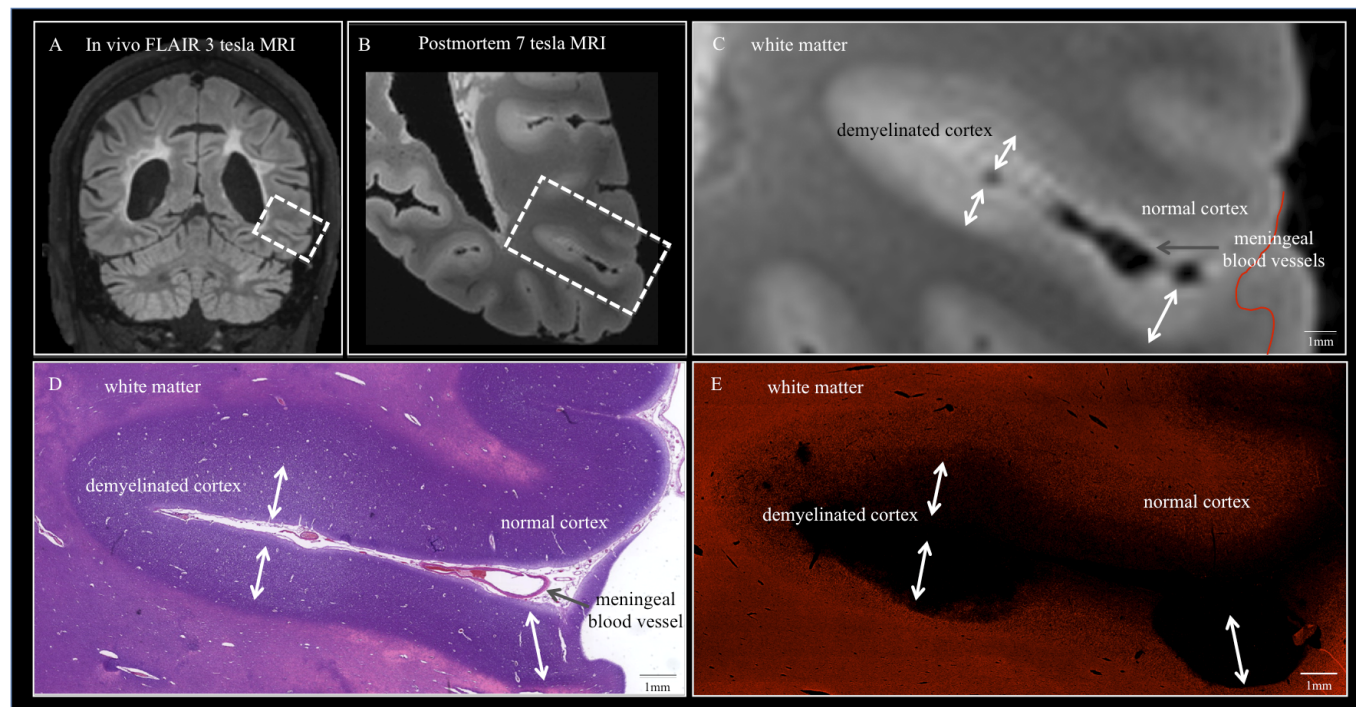


**FIGURE 4.** Multimodal MRI-histology examination. (**A–E**) A cortical MS lesion was barely visible on in vivo scans (**A**, boxed area) but clearly visible on the postmortem 3D GRE scan (**B**, white box). White arrows indicate the extent of cortical lesions on the GRE MRI image (**C**) and in histologic sections with H&E staining (**D**) and myelin PLP immunohistochemistry (**E**). The red line in (**C**) indicates where the fixed tissue was broken during slicing; this contour is evident in the right lower portion of (**D**).

temperature compound (Tissue-Tek; Sakura Finetek Europe BV, Alphen aan den Rijn, the Netherlands) for freezing and sectioning. Twenty-five 10- $\mu$ m-thick frozen sections were obtained on a sliding microtome cryostat and mounted on 1  $\times$  3-in glass slides, 6 of which were stained with hematoxylin and eosin (H&E) and Luxol fast blue–periodic acid Schiff and compared with the MRI from the same location. Stained sections were digitized at 20 $\times$  magnification using a slide scanner (iScan Coreo; Ventana Medical Systems Inc, Tucson, AZ). In addition, immunohistochemistry for myelin proteolipid protein (PLP), using mouse IgG2a anti-myelin PLP (ab118484; Abcam, Cambridge, MA) primary antibody and goat anti-mouse IgG2a-Alexa Fluor 647 (A21241; Invitrogen, Carlsbad, CA) secondary antibody, was performed on a representative frozen section to detect demyelinated cortical lesions. Further details are described in Supplemental Methods, Supplemental Digital Content 3, <http://links.lww.com/NEN/A614>.

Block 2 was obtained from Patient 2. The selected formalin-fixed tissue block from the left frontal lobe was processed routinely and embedded in paraffin; thirty 10- $\mu$ m-thick sections were obtained on a microtome. Six of the 30 paraffin-embedded sections were stained with H&E and Luxol fast blue–periodic acid Schiff and compared with the MRI (Figure, Supplemental Digital Content 4, <http://links.lww.com/NEN/A615>).

Block 3 was obtained from Patient 3. The selected formalin-fixed tissue block from the left hippocampus was processed routinely and embedded in paraffin; thirty 10- $\mu$ m-thick sections were obtained on a microtome. Four of the 30 paraffin-embedded sections were stained with H&E and

Cresyl violet and compared with the MRI (Figure, Supplemental Digital Content 5, <http://links.lww.com/NEN/A616>).

In all cases, H&E-stained sections were used for overall assessment of cellular changes, neuronal and neuroglial distributions, and cortical architecture. Sections stained with Luxol fast blue–periodic acid Schiff were used for assessment of myelin and demyelination. Cresyl violet–stained sections were used for assessing neuronal distribution in hippocampal sections.

## RESULTS

### Brain Sectioning With and Without Cutting Box

The postmortem brains were placed in the imaging container and immersed in Fomblin, after which air bubbles were aspirated and images were acquired at 7 T (Fig. 1A). Two brains underwent sectioning with the cutting box (Patients 1 and 3), and one brain underwent sectioning without the cutting box (Patient 2) (Table). The fixed brains fit without perceptible wobble or motion within the cutting box that was designed from the postmortem T1-MPRAGE images and printed on the 3D printer (Figs. 1B, C for the forebrain and brainstem-cerebellum, respectively, of Patient 1).

After sectioning, the gross anatomy of the anterior and posterior surfaces of each slab was easily matched ( $\sim$ 1 hour of labor for the entire brain) with the corresponding MRI slices (Fig. 2A, Patient 1; Figure, Supplemental Digital Content 6, <http://links.lww.com/NEN/A617>, Patient 3). Reformatting the MRI images in a transversal plane allowed visualization of

the thickness and skewness of the cutting planes. There were marked improvements in uniformity of thickness and skewness of the slabs with the cutting box (Fig. 2B, Patient 1) compared with the traditional sectioning method (Fig. 2C, Patient 2). In both brains sectioned with the cutting box, 1 cut was missed, resulting in 1 less slab than planned. The matches between the brain slab surface and MRI were not perfect for all slabs: 6 of 22 slab surfaces in Patient 1 (Fig. 2B, dotted lines) and 5 of 20 slab surfaces in Patient 3 were judged as not accurate. This was thought to be attributable to slight movement of the brain during the sectioning process.

By comparison, the performance of the traditional cutting method (Patient 2) was poor, with 13 of 15 approximately 1-cm-thick slabs (86%) judged to be nonparallel to one another and to the plane passing through the mammillary bodies (Fig. 2C). Matching of these slabs to the MRI was therefore extremely difficult and time-consuming, requiring approximately 12 hours of labor for the whole brain.

Figure, Supplemental Digital Content 2, <http://links.lww.com/NEN/A613>, offers a closer look at the match between MRI (T1-MPRAGE on the left) and the anterior and posterior surfaces of Slab 13 (Patient 1). Optimal registration was achieved using 2D coregistration between gray scale photos of the slice surfaces and corresponding slices on MRI.

### Brainstem-Cerebellum Sectioning With Cutting Box

Because of its success in improving the accuracy of the pathologic sectioning of the cerebral hemispheres, we considered whether the same approach could be applied to a more difficult problem: the brainstem-cerebellum (Patient 1). Two (25%) of 8 slabs were judged to be insufficiently accurate (Fig. 3, indicated by asterisk). As with cerebral sections, fine structures, including demyelinating lesions centered on prominent veins (Fig. 3, arrows), could be appreciated on the MRI scan (Fig. 3, in gray scale) and easily colocalized on gross examination (Fig. 3, colored photos). Direct comparison of the sectioning performance of the brainstem-cerebellum with (Patient 1) and without (Patients 2 and 3) cutting box is not available.

### MRI-Guided Histopathology

To assess the correspondence between high-resolution postmortem MRI and histopathologic findings, we chose a sulcus (Slab 18) in Patient 1 that appeared to harbor a cortical lesion on both in vivo and postmortem scans (Figs. 4A, B) (15–17). The lesion was better appreciated on the postmortem GRE T2\* (Figs. 4B, C) than on the in vivo images, probably owing to better resolution of the postmortem scan and fixation-related changes in MRI relaxation properties. Histologic characterization and comparison with MRI are shown in Figures 4C to E, where white arrows have been manually drawn to indicate the extent of the lesion and where a red line shows tissue missing from the histology image (lost during cryosectioning). Furthermore, the general shape of the sulcus, as well as the location, size, and shape of both the lesion and sulcal blood vessels, are extremely well matched between MRI and histologic analysis (Figs. 4C–E), demonstrating the accuracy of the technique. As shown with immunofluores-

cence staining for PLP, the normal myelin architecture of the cortex is disrupted at the level of the lesions because of the lesion that affects the cortex from the pial surface to the approximate location of cortical layers IV to V (Fig. 4E). This lesion can be classified as a type 3 subpial cortical lesion (18).

Similarly, histologic characterization and comparison with MRI were performed for hippocampal sections (Slice 13) in Patient 3 (with anti-*N*-methyl-D-aspartate receptor encephalitis) and shown in Figure, Supplemental Digital Content 5, <http://links.lww.com/NEN/A616>. Upon H&E and Cresyl violet staining, there were no remarkable histologic findings in the hippocampi of this patient.

For comparison, a third tissue block was sectioned in the left frontal lobe (Slab 6, Patient 2) of the brain that underwent the traditional cutting procedure (14). Histologic characterization and comparison with MRI *a posteriori* are shown in Figure, Supplemental Digital Content 4, parts A–D, <http://links.lww.com/NEN/A615>. Even with the larger section (i.e. 2 × 3-in vs 1 × 3-in glass slides; Figure, Supplemental Digital Content 4, <http://links.lww.com/NEN/A615>), which, in principle, would improve topographic localization, the match was less accurate and more time-consuming.

### DISCUSSION

Combining different expertise and multimodal approaches can advance our knowledge and understanding of the pathobiologic basis of different neurologic diseases. Here, using an individualized cutting box for fixed-brain tissue rather than traditional sectioning approaches, we show that an accurate multimodal integration between MRI and pathology is feasible in the research setting.

Postmortem MRI acquisition of fixed brain tissue is useful because it provides a more detailed view of brain structures and identifies minute findings that may have been missed in vivo; thus, it may facilitate better MRI-neuropathology analysis for clinical-pathologic correlations (8, 19). Nevertheless, postmortem scanning is challenging for several reasons. First, it needs to account for changes in T1 and T2 relaxation time constants caused by formalin fixation (20–25). Second, it is difficult, for technical reasons, to image the whole brain with multiple optimized imaging contrasts at high resolution in a single setting. Conventional studies of MRI-pathology correlations involve imaging slices of tissue after the initial cutting of the brain (1, 3, 5, 19, 21, 26). In such cases, higher-resolution scans can be performed on individual slabs at the same imaging time because of the limited coverage necessary. In our experience, several advantages prompt the preferential MRI acquisition of the whole brain over single or multiple approximately 1-cm-thick slabs; most important among these is the preservation of anatomic landmarks, which facilitates reliable comparison with longitudinal in vivo scans.

Our results clearly show that sectioning is superior with the cutting box (Figs. 2, 3; Figure, Supplemental Digital Content 6, <http://links.lww.com/NEN/A617>). Matching the pathologic sections and MRI scans was easy and rapid (~1 hour vs ~10–15 hours required after standard sectioning) because the comparison was direct and it was not necessary to reformat or resample the scan. After visual identification of



matching slices, further digital coregistration between MRI and pathology can correct residual inaccuracies, if necessary, before quantitative analysis. In addition, the targets assessed herein—a cortical MS lesion (Patient 1) (16, 17) detected on postmortem MRI (Fig. 4) and the hippocampus (Figure, Supplemental Digital Content 5, <http://links.lww.com/NEN/A616>)—were correctly localized after the pathologic cut in the expected slab and at the expected location. These targets were subsequently analyzed using standard histologic stains, confirming that a complete translational approach from in vivo to postmortem data is both feasible and valuable.

Mismatches between in vivo and postmortem MRI also arise because of distortions from subtle motion between hemispheres. For these reasons, care is required to identify the sulcus and other regions of interest in the postmortem images correctly. For histopathologic correlations, additional important sources of error can be the discrepancy between the thickness of the MRI slice and the histologic section, the related issue of volume averaging, and tissue shrinkage, which may be method-dependent. It has been reported that fixed tissue shrinks by 15% to 30% upon paraffin embedding (27), which would have to be accounted for when measuring the distance from the slab surface to the lesion of interest in MRI-guided histology. Although widely variable among tissue types, such shrinkage and distortion are reportedly less with the cryosectioning technique than with other procedures such as paraffin embedding (28).

The 3D cutting box method can be extended beyond what we report herein, for example, by changing the orientation of sections to match disease features or to reduce slab thickness below 6 mm. The design flexibility that is intrinsic to our approach is the major advantage over noncustomizable slicing boxes for brain hemispheres, which have been implemented in previous MRI-pathology correlation studies (4, 10). In this context, studies that require researchers to maintain the anatomic integrity of midline brain structures will benefit from the whole-brain approach.

Of note, the feasibility of this method is not limited by the strength of the MRI magnet used because the anatomic sequence used to design the cutting box (~6.5-minute 3D T1-MPRAGE) can be easily acquired on 1.5- and 3-T scanners. In our experience, a short training in the use of this device helps to minimize sectioning mistakes (e.g. missing, wavy, or incomplete cuts), as occurred for a few slabs in Patients 1 and 3. Simultaneous sectioning of all the slabs, instead of sequential cuts, might reduce skewness and other errors, but this would require a customized cutting device (e.g. multiple wires or knives set at interslice distance). Finally, in the implementation described here, we describe localization and histological analysis with small tissue blocks and 10- $\mu$ m-thick sections, rather than whole mounts. However, whole mounts could also be matched to the MRI in a similar way.

In conclusion, our approach embodies the concept that whole-brain postmortem MRI can facilitate and guide pathology, thereby providing a benchmark for comparison before and after sectioning. The use of an individually rendered, 3-dimensionally printed cutting box for fixed brains can improve the speed, quality, and accuracy of the pathologic localization of small lesions identified on MRI, such as those

commonly occurring in MS and many other brain diseases. The devices tested in this study (i.e. imaging container and cutting box) offer clear methodologic improvement, can be easily adapted for use in other brain disorders, and can be optimized according to specific research questions.

## ACKNOWLEDGMENTS

*We thank Dragan Maric (manager, Flow Cytometry Core Facility, National Institute of Neurological Disorders and Stroke) for helping with myelin PLP immunohistochemistry. We thank Afonso Silva for inspiring this idea, Thomas Talbot for assistance with the 3D printer, Southail Inati and Hellmut Merkle for technical advice, Nancy Edwards for pathologic advice, and Dr David Nauen for helping with brain sectioning at Johns Hopkins University. We are deeply grateful to our patients and their families for their willingness to participate in organ donation and to authorize autopsy procedures for biomedical research.*

## REFERENCES

- Schmierer K, Scaravilli F, Altmann DR, et al. Magnetization transfer ratio and myelin in postmortem multiple sclerosis brain. *Ann Neurol* 2004;56:407–15
- Schmierer K, Tozer DJ, Scaravilli F, et al. Quantitative magnetization transfer imaging in postmortem multiple sclerosis brain. *J Magn Reson Imaging* 2007;26:41–51
- Schmierer K, Wheeler-Kingshott CA, Boulby PA, et al. Diffusion tensor imaging of post mortem multiple sclerosis brain. *Neuroimage* 2007;35:467–77
- Moll NM, Cossoy MB, Fisher E, et al. Imaging correlates of leukocyte accumulation and CXCR4/CXCL12 in multiple sclerosis. *Arch Neurol* 2009;66:44–53
- Seewann A, Kooi EJ, Roosendaal SD, et al. Translating pathology in multiple sclerosis: The combination of postmortem imaging, histopathology and clinical findings. *Acta Neurol Scand* 2009;119:349–55
- Annese J, Schenker-Ahmed NM, Bartsch H, et al. Postmortem examination of patient H.M.'s brain based on histological sectioning and digital 3D reconstruction. *Nat Commun* 2014;5:3122
- Annese J. The importance of combining MRI and large-scale digital histology in neuroimaging studies of brain connectivity and disease. *Front Neuroinform* 2012;6:13
- Schmierer K, Scaravilli F, Barker GJ, et al. Stereotactic co-registration of magnetic resonance imaging and histopathology in post-mortem multiple sclerosis brain. *Neuropathol Appl Neurobiol* 2003;29:596–601
- Bo L, Geurts JJ, Ravid R, et al. Magnetic resonance imaging as a tool to examine the neuropathology of multiple sclerosis. *Neuropathol Appl Neurobiol* 2004;30:106–17
- Fisher E, Chang A, Fox RJ, et al. Imaging correlates of axonal swelling in chronic multiple sclerosis brains. *Ann Neurol* 2007;62:219–28
- Boyko OB, Alston SR, Fuller GN, et al. Utility of postmortem magnetic resonance imaging in clinical neuropathology. *Arch Pathol Lab Med* 1994;118:219–25
- Ruder TD, Thali MJ, Hatch GM. Essentials of forensic post-mortem MR imaging in adults. *Br J Radiol* 2014;87:20130567
- Pollanen MS, Woodford N. Virtual autopsy: Time for a clinical trial. *Forensic Sci Med Pathol* 2013;9:427–28
- Powers JM. Practice guidelines for autopsy pathology. Autopsy procedures for brain, spinal cord, and neuromuscular system. Autopsy Committee of the College of American Pathologists. *Arch Pathol Lab Med* 1995;119:777–83
- Pitt D, Boster A, Pei W, et al. Imaging cortical lesions in multiple sclerosis with ultra-high-field magnetic resonance imaging. *Arch Neurol* 2010;67:812–18
- Popescu BF, Lucchinetti CF. Meningeal and cortical grey matter pathology in multiple sclerosis. *BMC Neurol* 2012;12:11
- Daams M, Geurts JJ, Barkhof F. Cortical imaging in multiple sclerosis: Recent findings and 'grand challenges'. *Curr Opin Neurol* 2013;26:345–52



18. Kidd D, Barkhof F, McConnell R, et al. Cortical lesions in multiple sclerosis. *Brain* 1999;122:17–26
19. Geurts JJ, Bo L, Pouwels PJ, et al. Cortical lesions in multiple sclerosis: Combined postmortem MR imaging and histopathology. *AJNR Am J Neuroradiol* 2005;26:572–77
20. Blamire AM, Rowe JG, Styles P, et al. Optimising imaging parameters for post mortem MR imaging of the human brain. *Acta Radiol* 1999;40:593–97
21. Pfefferbaum A, Sullivan EV, Adalsteinsson E, et al. Postmortem MR imaging of formalin-fixed human brain. *Neuroimage* 2004;21:1585–95
22. Yong-Hing CJ, Obenaus A, Stryker R, et al. Magnetic resonance imaging and mathematical modeling of progressive formalin fixation of the human brain. *Magn Reson Med* 2005;54:324–32
23. Schmierer K, Wheeler-Kingshott CA, Tozer DJ, et al. Quantitative magnetic resonance of postmortem multiple sclerosis brain before and after fixation. *Magn Reson Med* 2008;59:268–77
24. Dawe RJ, Bennett DA, Schneider JA, et al. Postmortem MRI of human brain hemispheres: T2 relaxation times during formaldehyde fixation. *Magn Reson Med* 2009;61:810–18
25. Schmierer K, Thavarajah JR, An SF, et al. Effects of formalin fixation on magnetic resonance indices in multiple sclerosis cortical gray matter. *J Magn Reson Imaging* 2010;32:1054–60
26. Schmierer K, Parkes HG, So PW. Direct visualization of remyelination in multiple sclerosis using T2-weighted high-field MRI. *Neurology* 2009;72:472
27. Boonstra H, Oosterhuis JW, Oosterhuis AM, et al. Cervical tissue shrinkage by formaldehyde fixation, paraffin wax embedding, section cutting and mounting. *Virchows Arch A Pathol Anat Histopathol* 1983;402:195–201
28. West MJ. *Basic Stereology for Biologists and Neuroscientists*. Cold Spring Harbor, NY: CSHL Press, 2012